FZD-544

Preliminary investigations on high energy electron beam tomography

Yves Bärtling, Dietrich Hoppe,
Uwe Hampel

Dezember 2010

Wissenschaftlich-Technische Berichte
FZD-544 2010 · ISSN 1437-322X

WISSENSCHAFTLICH-TECHNISCHE BERICHTE

Forschungszentrum
Dresden Rossendorf

Wissenschaftlich-Technische Berichte
FZD-544
Dezember 2010

Uwe Hampel, Dietrich Hoppe, Yves Bärtling

Preliminary investigations on high energy electron beam tomography

Forschungszentrum
Dresden Rossendorf

Forschungszentrum
Dresden Rossendorf

Report

Preliminary investigations on high energy electron beam tomography

Project partner
Budker Institute of Nuclear Physics,
Akademik Lavrent'ev av. 11,
630090 Novosibirsk
Russia

Project leader (FZD)
Uwe Hampel
Institute of Safety Research

Responsible scientists (FZD)
Dietrich Hoppe, Yves Bärtling
Institute of Safety Research

Date of report submission
10/11/2010

Table of contents

1 Project objectives

In computed tomography (CT) cross-sectional images of the attenuation distribution within a slice are created by scanning radiographic projections of an object with a rotating X-ray source-detector compound and subsequent reconstruction of the images from these projection data on a computer. CT can be made very fast by employing a scanned electron beam instead of a mechanically moving X-ray source. Based on this principle Forschungszentrum Dresden-Rossendorf (FZD) has already built a dedicated X-ray tomography scanner for flow imaging being able to provide up to 7000 slice images per second at a spatial resolution of ~1 mm and a tube voltage of 150 kV [1, 2].
Now this principle should be extended towards high-energy electron beam tomography with an electrostatic accelerator. Therefore a dedicated experimental campaign was planned and carried out at the Budker Insitute of Nuclear Physics (BINP), Novosibirsk. There we investigated the capabilities of BINP's accelerators as an electron beam generating and scanning unit of a potential high-energy electron beam tomography device.

The study addressed the following essential issues:

1. What is the efficiency and signal-to-noise ratio (SNR) of the detector?
2. What are the parameters of the electron beam and the focal spot (spot size, deflection pattern accuracy, ripples, drift)?
3. What are the quality parameters of CT images (spatial resolution, contrast, SNR) for typical beam energies, intensities, and detector bandwidths?

2 Experimental setup

2.1 General setup

An electron beam tomography setup usually consists of a circular X-ray target and a circular detector. The electron beam scans along the target and thus the focal spot creates a rotating X-ray source. A circular X-ray detector then acquires the projection data. For the experiments reported here this general setup was simplified to perform a proof-of-principle with reasonable effort. The setup is shown in Figure 1. For the study we used an ELV-6 accelerator (Figure 2). ELV type accelerators made by BINP are typically used for polymer modification, sewage water treatment, purification of flue gases or insect control of grain. ELV accelerators are electrostatic accelerators with a cascaded transformer principle. A single primary winding of the transformer induces 20 kV alternating voltage in a set of secondary windings. At the secondary winding stages the voltage is doubled, rectified and cascaded along an accelerator column to the desired total acceleration voltage. For ELV-6 the acceleration tube is inside the transformer within a single SF6 gas pressure vessel. For some other accelerators the transformer and accelerator tube are in separate housings. The cathode is a thermionic electron source operated with a dc heating current. The latter adjusts the cathode current. There is no Wehnelt control of the electron current. Typical parameters of ELV accelerators are given in Table 1.

The ELV-6 accelerator was modified to perform principle CT studies. We kept the beam horn which is typically used to extract the electron beam across a larger area but replaced the Ti-foil and electron beam extraction window by an aluminium plate which served as a target holder and X-ray extraction window (Figure 3). As a target we used a 600 mm × 18 mm × 0.4 mm tantalum strip which was fixed inside the beam horn on the aluminium plate.

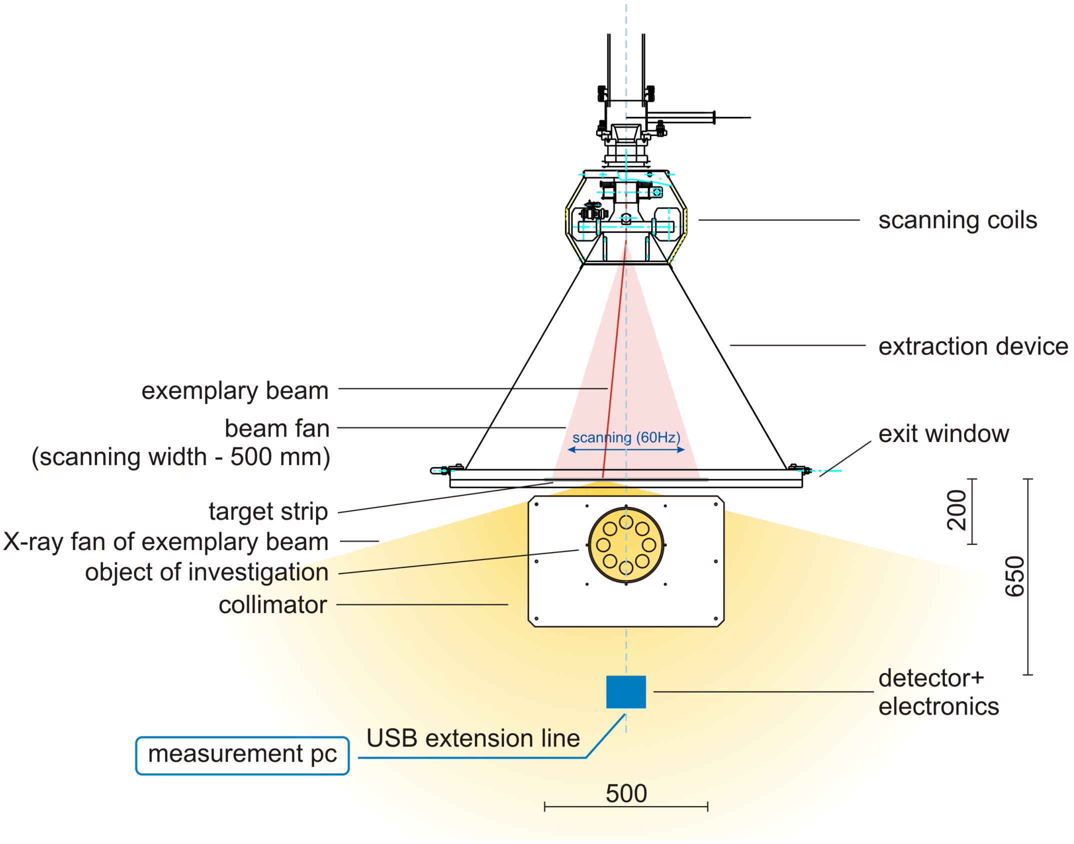

Figure 1: Schematic of experimental setup and electron beam scanning.

The focussed electron beam was linearly scanned at 60 Hz frequency across this target by means of an electromagnetic coil system. An extra focussing lens was added to the conventional setup to provide beam focussing, which is usually not required. A single X-ray detector was placed 650 mm underneath the target in the direction of the electron beam axis. The detector recorded the intensity of the incoming X-rays with a rate of up to 200 kS/s. The object of investigation was placed between target and detector. In this study the object was mechanically rotated with 6 rpm in order to create CT projection data.

Table 1: Parameters of ELV electron accelerators [3].

ELV type	**Energy range [MeV]**	**Beam power [kW]**	**Max. beam current [mA]**
ELV-mini	0.2 – 0.4	20	50
ELV-0.5	0.4 – 0.7	25	40
ELV-1	0.4 – 0.8	25	40
ELV-2	0.8 – 1.5	20	25
ELV-3	0.5 – 0.7	50	100
ELV-4	1.0 – 1.5	50	100
ELV-6	0.8 – 1.2	100	100
ELV-8	1.0 – 2.5	90	50
ELV-6M	0.75 – 0.95	160	200
ELV-12	0.6 – 1.0	400	400

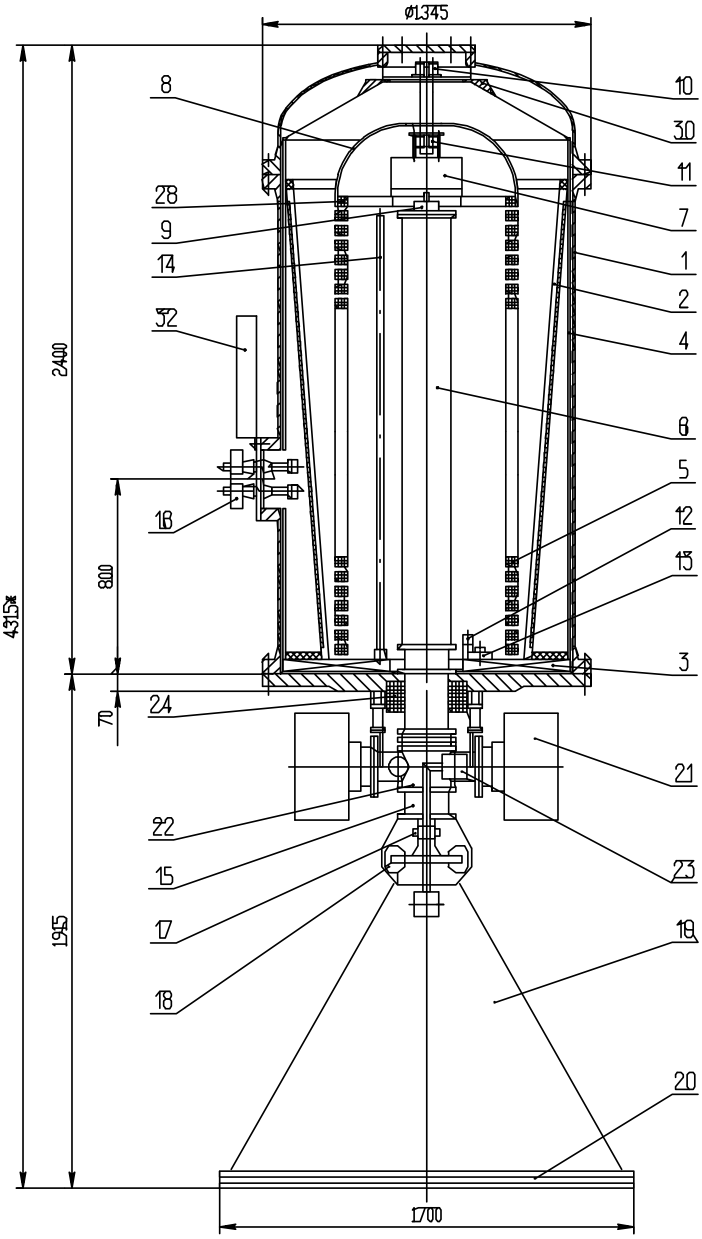

Figure 2: Schematic of an ELV-accelerator [3].

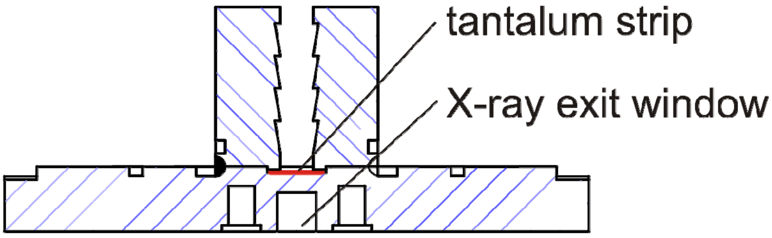

Figure 3: Cross sectional view of the modified extraction window and the tantalum inlay.

To reduce scattered radiation we provided collimation of the X-ray fan by an arrangement of two parallel steel plates in beam direction that faced each other at a distance of 10 mm. The object of investigation was placed and rotated within a ∅ 230 mm cut-out in these plates (Figure 4).

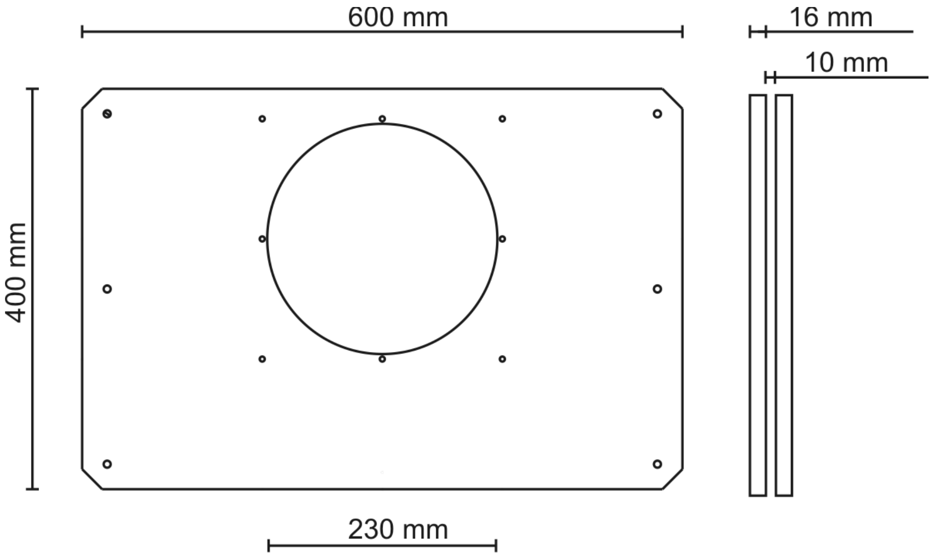

Figure 4: Front and side view of the collimator (600 mm × 400 mm).

In order to obtain the complete set of projections for the tomography the phantoms have to be rotated at a known speed. Therefore a rotary stage was constructed that fits easily to the given collimator and allows for sufficiently low spin speeds of about 6 rpm (Figure 5). In order to obtain precise information of the momentary spin speed a motor-encoder combination was used.

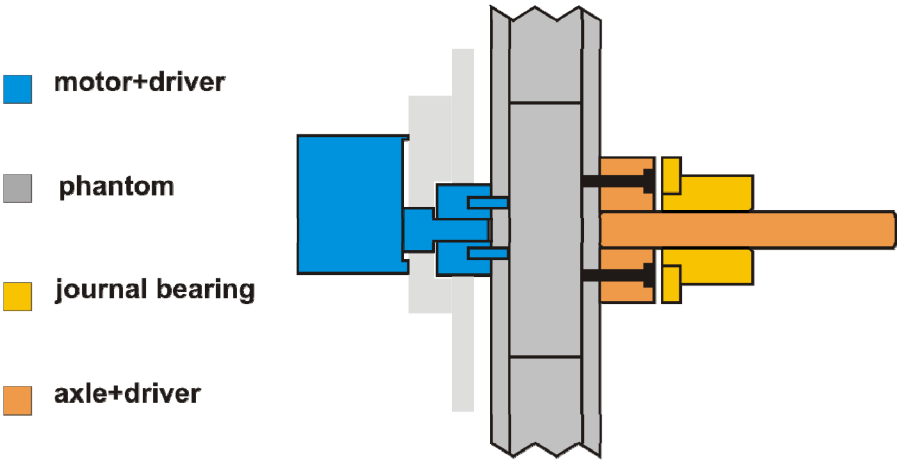

Figure 5: Rotary stage.

2.2 Detector and data acquisition

The intensity of the incoming X-rays was recorded with a single detector. Two different detector types have been tested during the experiments: Cadmium telluride (CdTe) solid state detectors and lutetium oxyorthosilicate (LSO) crystals coupled to an avalanche photo diode (APD). CdTe offers good temporal response and low pair creation energy, but suffers from drift effects and polarisation at high photon flux. It is already successfully used in “low-energy” (150 kV) ultrafast X-ray computed tomography systems at FZD. LSO-APD detectors provide better temporal response and have the advantage of a tuneable “built-in” amplification due to the characteristics of the APD. However they are more sensitive to changes in temperature and have lower conversion efficiency.
We tested the following detectors with different dimensions and slightly different material configurations (see Figure 6):

APD-LSO	LSO (1.6 x 3.2 x 5 mm^3) + APD
CdTe-Di-4×4	CdTe (4 x 4 x 1 mm^3), Pt-CdTe-In configuration
CdTe-2×5	CdTe (2 x 5 x 2 mm^3)
CdTe-Di-3×3	CdTe (3 x 3 x 2 mm^3), Pt-CdTe-In configuration.

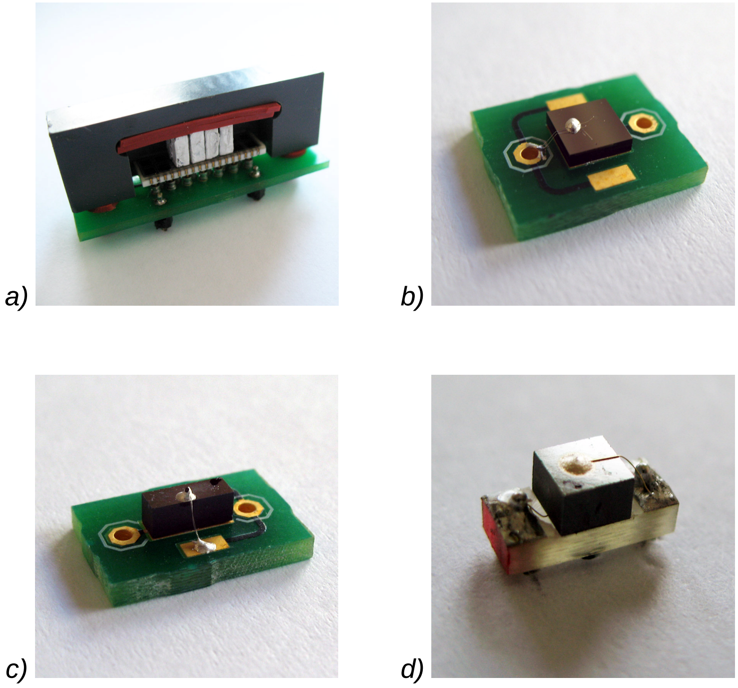

Figure 6: X-ray detectors used in the experiments
(a) APD-LSO, b) CdTe-Di-4×4, c) CdTe-2×5, d) CdTe-Di-3×3).

To meet the requirements for two different types of measurements it was necessary to employ detectors with different temporal response. For measurements where a high temporal resolution was required an amplifier circuit with an amplification of $570 \cdot 10^3$ V/A was used, allowing measurements of signals up to 3 MHz bandwidth. In order to digitise the data an 8-bit oscilloscope with a resolution of 39.1 mV per bit at ±5V, 15.6mV per bit at ±2V and 7.8mV per bit at ±1V was used. Since this oscilloscope is not able to continuously stream data a 16-bit data acquisition card (Goldammer – USB Basic/Sim light OEM, G0S-1034-9) with 200 kS/s maximum acquisition rate was used for streaming measurements and the detector electronics was adapted adequately. The cut-off frequency of the amplifier for streaming measurements was set to 80 kHz and amplification of this circuit is $2500 \cdot 10^3$ V/A. A resolution of 310 µV per bit can be achieved with this circuit.

In both concepts the digitised data was transmitted to the measurement PC by means of a USB (universal serial bus) connection. A USB extender (icron – USB Ranger 2104) with 30 m CAT-5 cable was utilised to cope with the long (~50 m) distance between the setup in the accelerator hall and the PC and the operator's room, since USB is normally only capable to passively bridge a distance of 5 m.

2.3 Phantoms

Two phantoms of different complexity have been designed and manufactured. The less complex one is a 195 mm diameter disc of PMMA (polymethyl methacrylate) surrounded by a metal ring made of aluminium (Figure 7). Within the disc there are six holes of 30 mm diameter containing four (removable) metal inserts. PMMA was used for the disc since it has a similar attenuation as water.

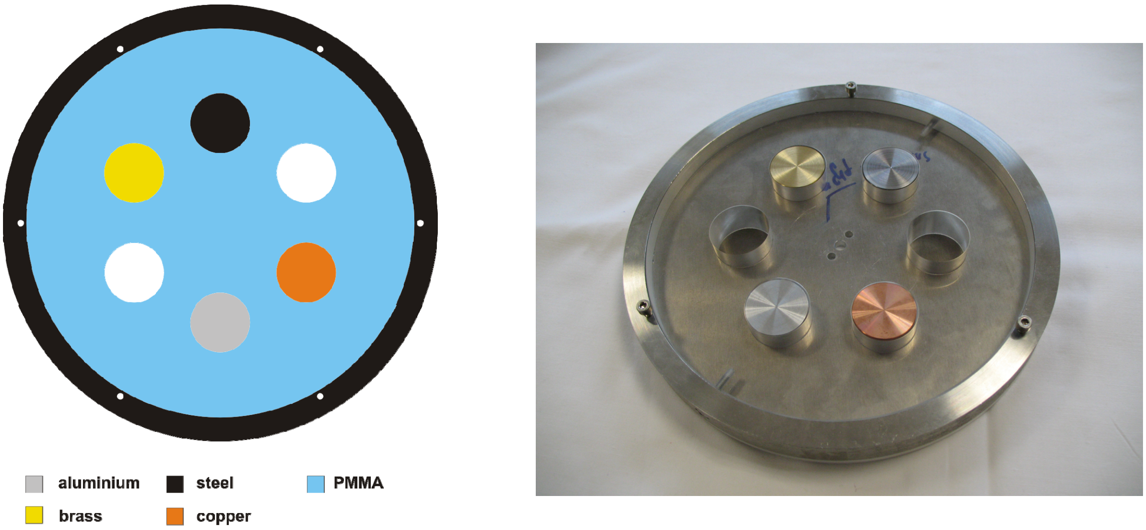

Figure 7: PMMA phantom with outer metal ring and inserts a) schematic and b) photo.

The second phantom (Figure 8) has a more complex structure which was adopted from a nuclear fuel element. The phantom resembles a pressure vessel (metal ring) with water (PMMA) and a fuel rod bundle inside. The bundle phantom is divided into four sectors:

1. top left (gas film):
    PMMA body and hollow pins surrounded by small air gaps (0 mm – 4 mm)
2. top right (gas bubbles):
    PMMA body with through holes (∅ 1 mm – 7 mm) and hollow pins
3. bottom left (liquid film):
    hollow pins surrounded by PMMA ferrules (outer-∅ 11 mm – 14 mm)
4. bottom right (drops):
    hollow pins and PMMA rods (∅ 1 mm – 7 mm).

The pins (fuel rods) have an inner diameter of 9 mm and a wall thickness of 1 mm. Close to the phantom's centre there is a square steel structure (35 mm edge length) with a through hole (∅ 25 mm) resembling a water channel. The inner part of the model is surrounded by a 2 mm thick metal band simulating a metal casing as shown in the schematic. The outer ring for this model is made of 6 mm thick aluminium

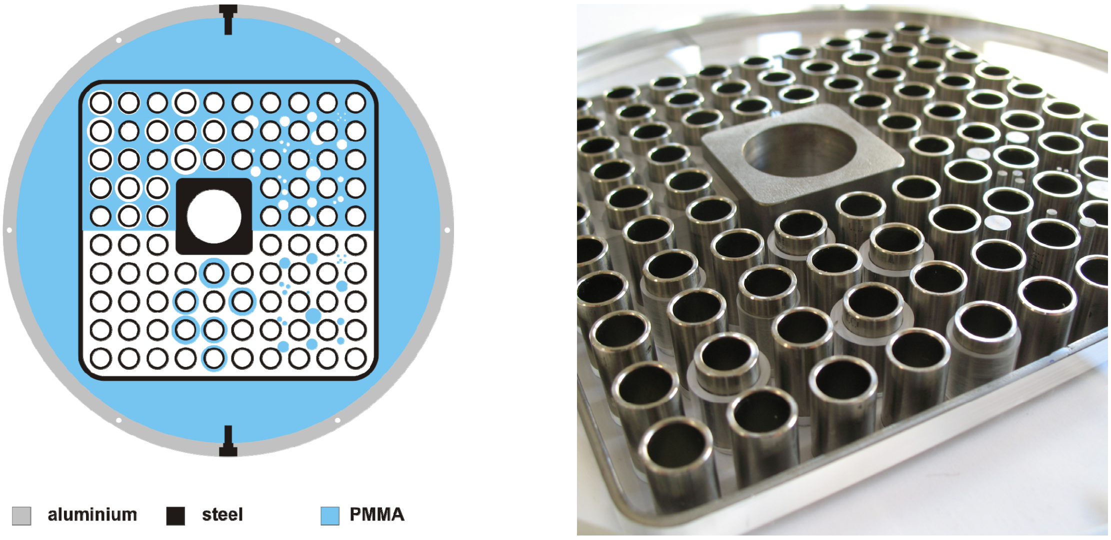

Figure 8: Fuel element phantom a) schematic and b) photo.

3 Experiments and results

3.1 General observations – reference measurement

In a first scan we measured the X-ray intensity with no object. This served as a performance check but also as a reference measurement for tomography. Figure 9 shows a trace of the detector signal. The X-ray intensity varies with the distance of the focal spot from the detector and is also influenced by the aluminium material in the path. The electron beam is periodically deflected at a frequency of approximately 60 Hz. The asymmetry in the detector signal curve is due to some eccentric alignment of the detector.

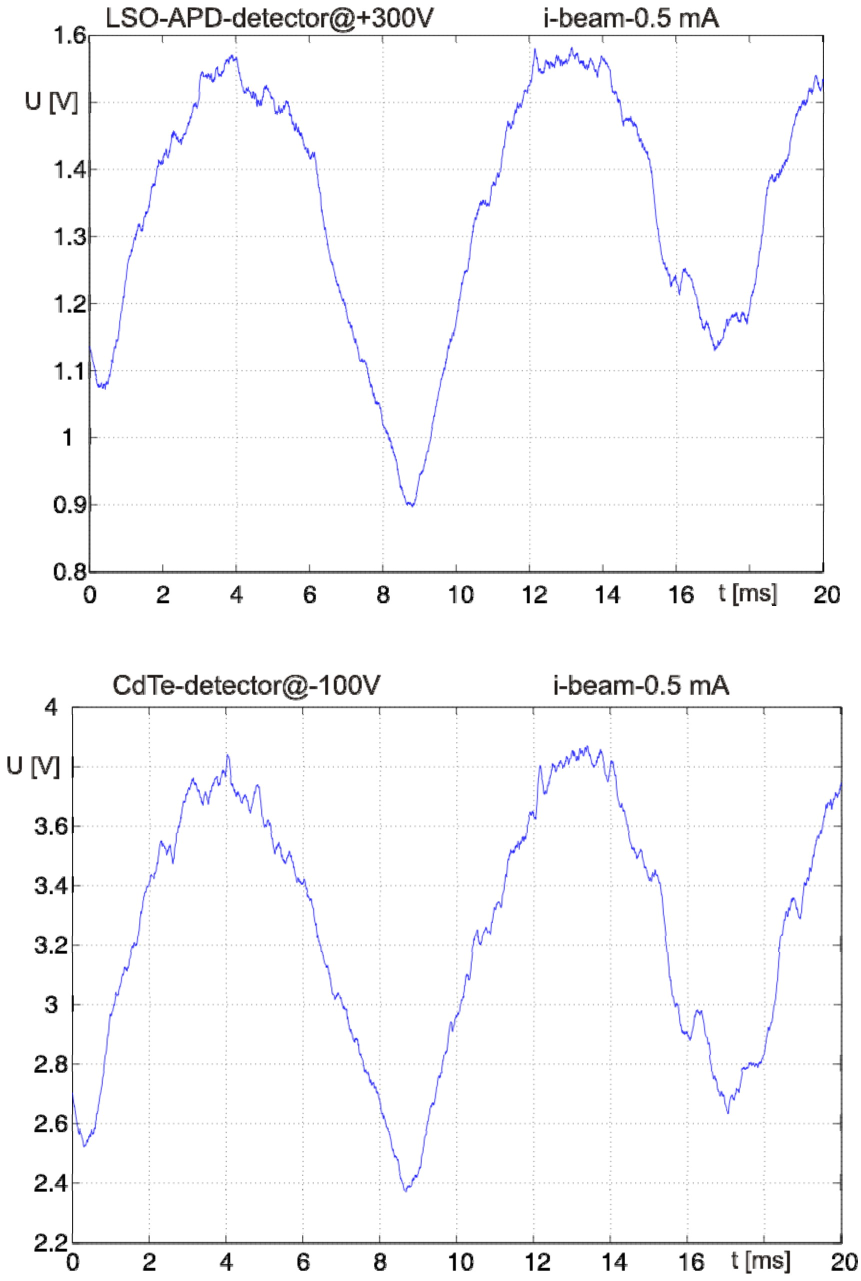

Figure 9: Amplified and offset compensated signal of detectors without object in path of rays top) LSO-APD detector, bottom) CdTe detector (2 × 5 × 2 mm³).

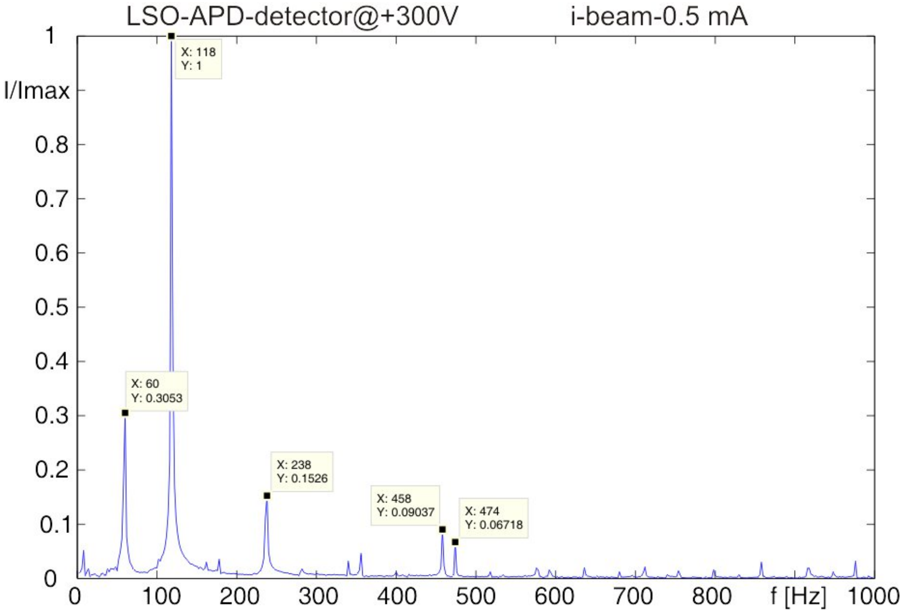

Figure 10: Frequency spectrum of LSO-APD signal.

A noticeable characteristic of the signal is the occurrence of periodic components (see frequency spectrum of the signal in Figure 10). There are harmonics from the scanning frequency (~60 Hz, ~118 Hz, ~238 Hz, ~474 Hz) and an additional harmonic at ~458 Hz which is obviously high voltage ripple that leads to unwanted harmonic electron beam deflection due to chromatic lens aberration.

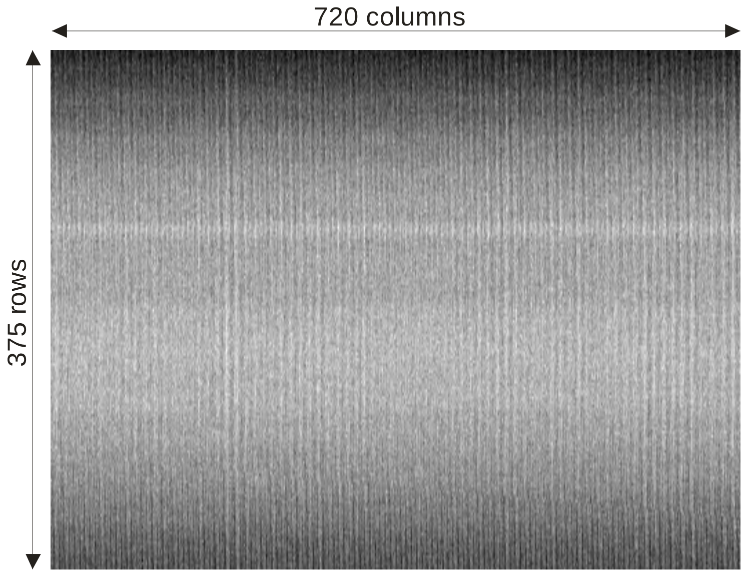

Figure 11: Grey value encoded reference data (375 rows, 720 columns [projections]).

The recorded data set was processed for use as reference data for the tomographic experiments. Therefore projections were separated from the serial data stream and each of them corresponds to a single period (as shown in Figure 9). The projections were then assembled as the columns of a matrix (sinogram) where the rows correspond to the beam position on the target. The resulting data matrix is shown in Figure 11 and the average of all projections is depicted in Figure 12.

During a single period the beam passes each position on the target twice due to the triangular deflection signal. Consequently the same set of information is recorded twice. To compensate for that only the first half of each period was used for the rows of the matrix.

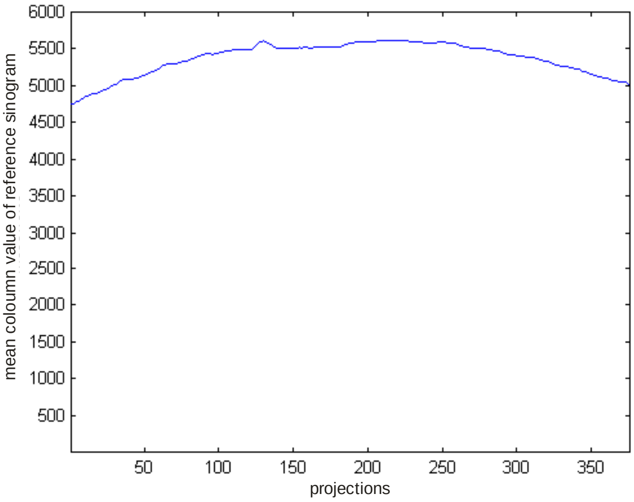

Figure 12: Average of all projections from the reference matrix.

3.2 Noise and repeat accuracy

In order to asses the signal quality it is important to understand the sources of noise within the system. There are two sources of signal fluctuation:

- noise originating from the detector-amplifier unit (stochastic);
- fluctuations in electron beam position (due to high voltage ripples) and beam intensity (systematic, but in this study difficult to measure).

The latter is a result of the accelerator's operation principle – electrons are emitted by a heated cathode and therefore undergo thermal noise. High voltage ripples lead to unwanted fluctuations of the beam deflection due to chromatic aberration of the lens.
The detector-amplifier unit is exposed to thermal noise (operational amplifiers, avalanche photo diodes) and experiences statistical signal fluctuations at low beam intensity. In order to determine the noise level of the detector-amplifier system two different concepts have been applied. The first one excludes any influence from the X-ray source by simply deriving the "dark noise level" – with no signal (X-ray) at the detector (refer to Figure 13). The other method determined the noise level at a given dc-like X-ray signal – thus it was possible to obtain the noise level by subtracting the averaged signal from the measured signal. However, this SNR depicts more the SNR of the source-detector compound rather than of the detector-amplifier unit itself. The SNR was calculated according to

$$SNR = 20 \cdot \log\left(\frac{U_{dc}}{U_{RMS-noise}}\right). \tag{1}$$

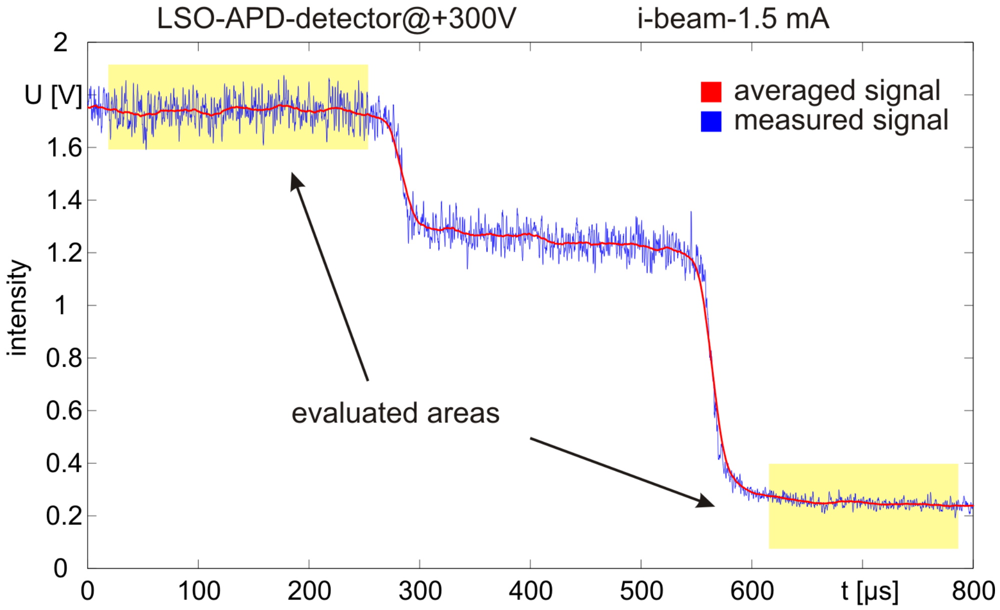

Figure 13: Methodology to determine the SNR from full-exposure (left part of curve) and no-exposure (right part of curve) raw intensity signals.

The results of the measurement are given in Table 2. The streaming-unit has a higher SNR than the fast acquisition unit which is related to the lower cut-off frequency at 80 kHz that is obtained by applying an active fifth-order low-pass filter (the other amplifier only had a second-order low-pass with cut-off frequency of 3 MHz). Another reason for the better performance might be the galvanic isolation between the analogue and the digital part of the data acquisition module. Consequently disturbances in the (digital) data transmission line did not affect the analogue part. The fact that the SNR increases at higher intensities is attributed to quantum noise at the detector.

Table 2: SNR of the beam-detector compound.

	Fast acquisition unit	**Streaming unit**
„Dark noise“ $U_{\text{noise-peak-to-peak}}$ / $U_{\text{noise-RMS}}$	80 mV / 14 mV	8 mV / 0.95 mV
Noise at “low signal level” $U_{\text{noise-RMS}}$ (@ U_{low})	14 mV (@0.25V) → SNR = 25 dB	21 mV (@1.23V) → SNR = 35 dB
Noise at “high signal level” $U_{\text{noise-RMS}}$ (@ U_{high})	45 mV (@1.7V) → SNR = 31.5 dB	38 mV (@4.10V) → SNR = 40.5 dB

In order to evaluate the repeat accuracy for periodic beam scanning a stream of data from 200 beam sweeps was recorded and overlaid (Figure 14). The common point is set at 0 ms and the time shift was measured at 4.65 ms. Figure 15 gives a detailed view of the temporal fit. The beam shifted approximately 100 µs during a set of 200 measurements which equals a total measurement time of 3333 ms. Assuming a constant deflection of 1000 mm at a frequency of 60 Hz this comes down to a maximum dislocation of the beam’s position of 6 mm.

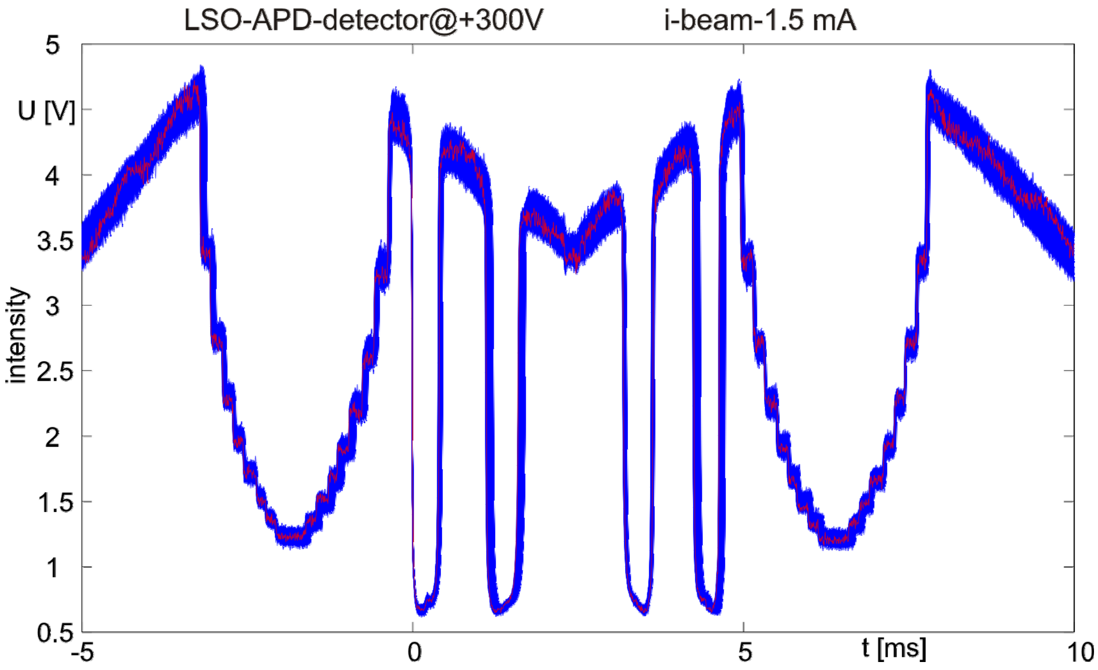

Figure 14: Overlaid intensity data for 200 beam sweeps.

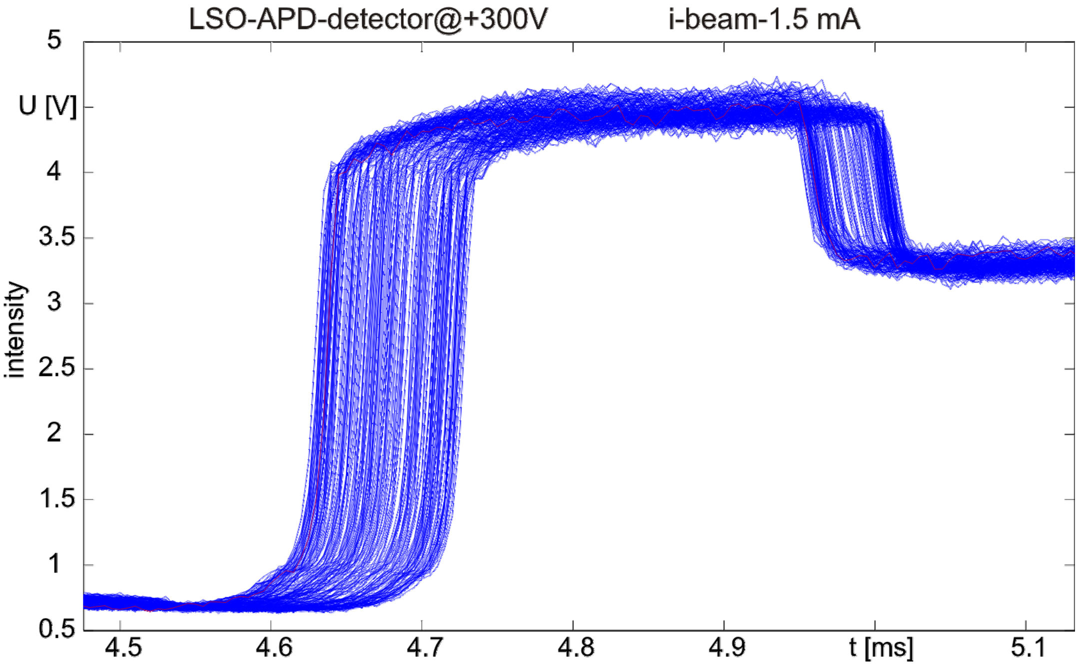

Figure 15: Temporal repeat accuracy – detailed view.

3.3 Step function response

The spot size of the X-ray source is a crucial parameter for the resolution of a tomographic measurement. To measure the focal spot diameter the setup shown in Figure 16 was used. Two sheets of tantalum and lead were placed in front of the X-ray exit window to partially obstruct the X-ray fan. When the beam disappeared behind the absorber edges the X-ray intensity at the detector changed in a step-like way (Figure 17). This step function can be analysed to estimate the focal spot diameter.

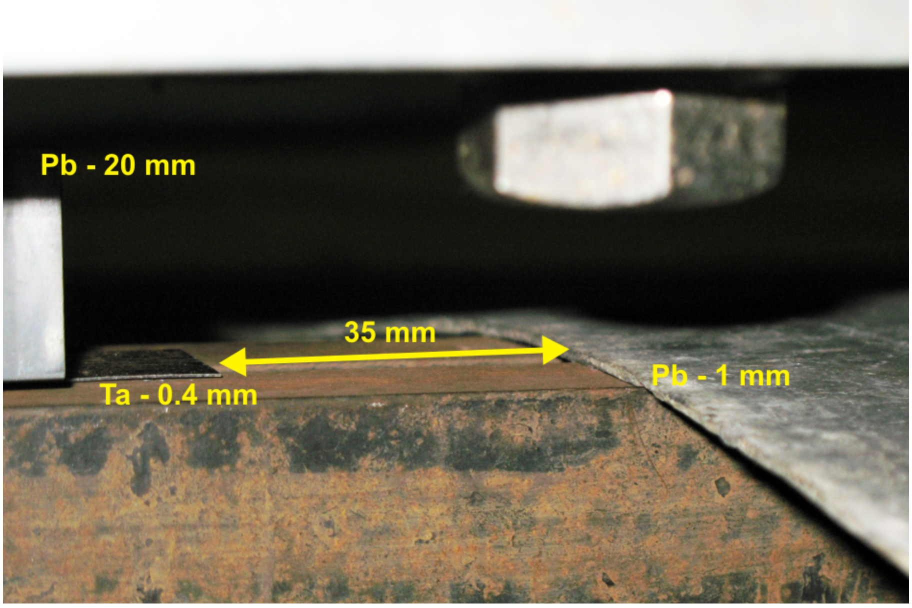

Figure 16: Setup for measurement of beam diameter.

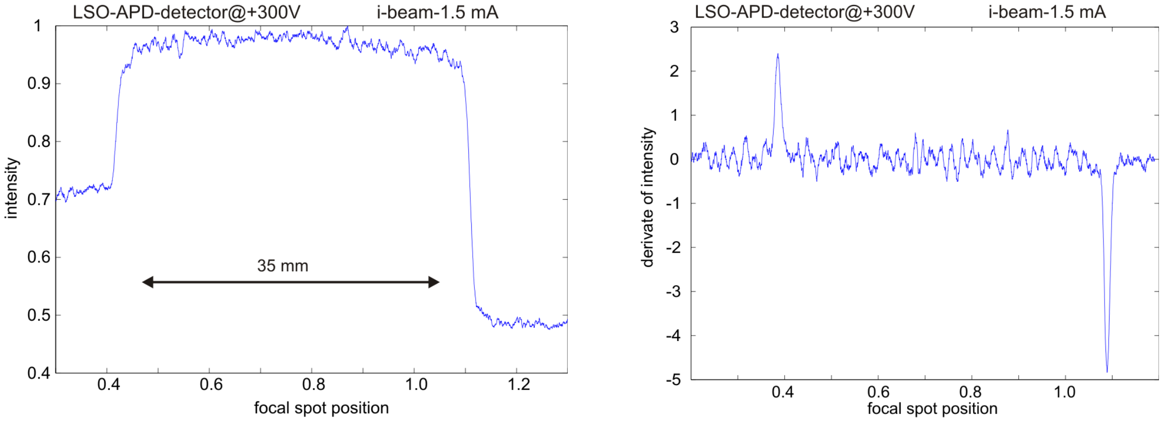

Figure 17: Raw signal (left) and signal derivative (right) for the step function measurement.

The derivative of the step response was calculated and the width of the maximum and minimum was analysed (Figure 17). They correspond to the time the beam takes to completely enter or leave the section without absorbers. Assuming a constant beam speed (1000 mm at 60 Hz) the beam width (FWHM – full width at half maximum) can be taken directly from the chart. Table 3 shows the results obtained from several measurements with different detectors. The variations for a single detector are due to the distortions in the beam deflection. The variations between different detectors are due to the different (temporal) characteristics of the detectors. It corresponds to the response time (10% to 90% of intensity change) and is illustrated in Table 3. The APD-LSO detector has shown the best temporal behaviour and was therefore selected for the following measurements.

Table 3: Beam dimensions obtained from step function response.

Detector type	N° of processed signals	Average response time [µs]	Minimum FWHM [mm]	Maximum FWHM [mm]	Average FWHM [mm]
APD-LSO					
Local max	15	30.8	0.475	1.075	0.646
Local min	15	31.3	0.610	0.941	0.734
CdTe-2×5					
Local max	15	36.4	0.586	1.018	0.776
Local min	15	36.9	0.701	0.994	0.823
CdTe-Di-4×4					
Local max	19	32.7	0.528	0.898	0.663
Local min	19	32.4	0.566	0.893	0.695
CdTe-Di-3×3					
Local max	19	35.4	0.475	0.850	0.638
Local min	19	31.3	0.590	0.888	0.696
Total	**136**	**33.4**	**0.566**	**0.945**	**0.709**

3.4 Linearity check by means of a wedge-like absorber

X-ray tomography is a technique to visualise areas with different density/attenuation properties. It relies on a linear relation between attenuation values along the beam and the integral beam attenuation, that is, the logarithm of the X-ray intensity. The intensity I of an X-ray after transmission through material of thickness x and attenuation coefficient μ is given by the exponential decay law

$$I = I_0 e^{-\mu x}. \tag{2}$$

The attenuation coefficient μ depends on the material and the photon energy (Figure 18).

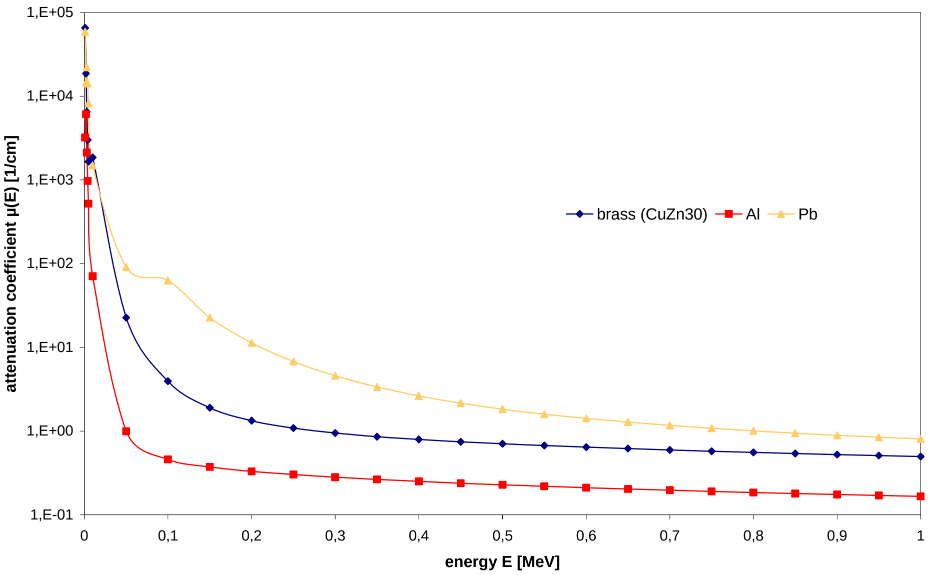

Figure 18: Attenuation coefficient of different materials.

The attenuation coefficient does not depend linearly on the energy and consequently high energy photons are less attenuated by material in the path of rays than low energy photons, which is commonly referred to as beam hardening.

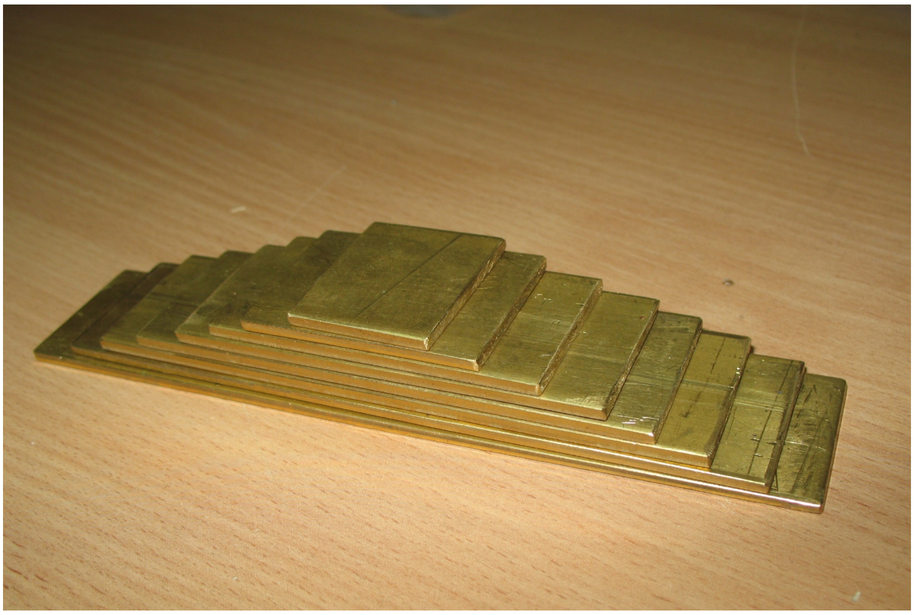

Figure 19: Wedge-shaped absorber made of 3mm brass plates.

To assess the linearity of the X-ray attenuation a wedge-shaped brass absorber (Figure 19) was placed underneath the X-ray extraction window. The intensity at the detector was recorded while the electron beam was deflected along the target strip. Two lead bricks (20 mm × 30 mm × 30 mm) were placed into the path of X-rays as “references”. The intensity signals from the detector are depicted in Figure 20. Both the brass body as well as the lead bricks are clearly recognisable. Due to the changing distance between the source spot and the detector there is no constant maximum intensity I_0.

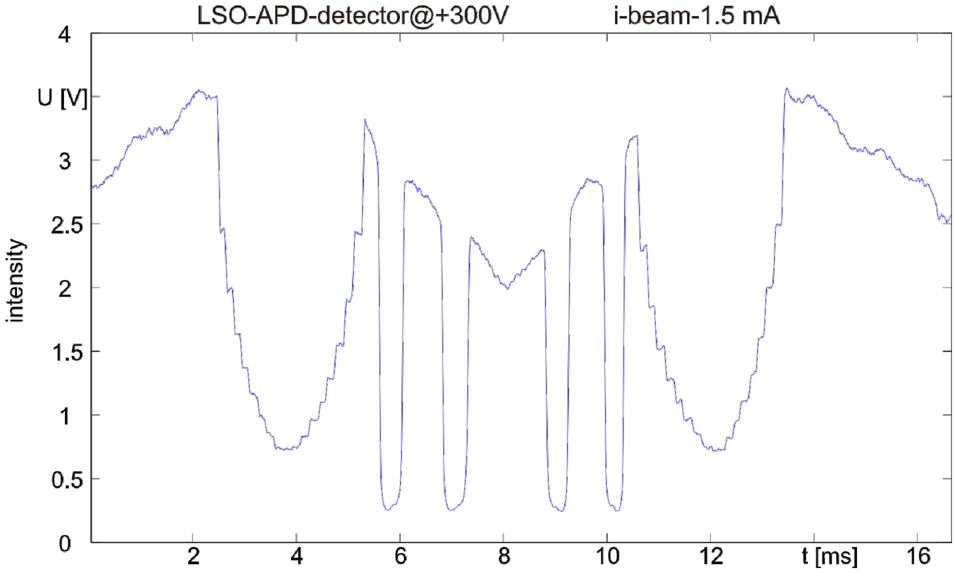

Figure 20: Intensity signal from with a wedge-like brass absorber.

To compensate for that a function was introduced which is given by

$$I_{0-corr} = \frac{a}{r^2} - b = \frac{a}{d_{sd}^2 + x^2(t)} - b, \qquad (3)$$

where *r* is the distance between source and detector, d_{sd} the distance between target strip and detector (approx. 650 mm) and *x* the time-dependent position of the source spot along the target strip.

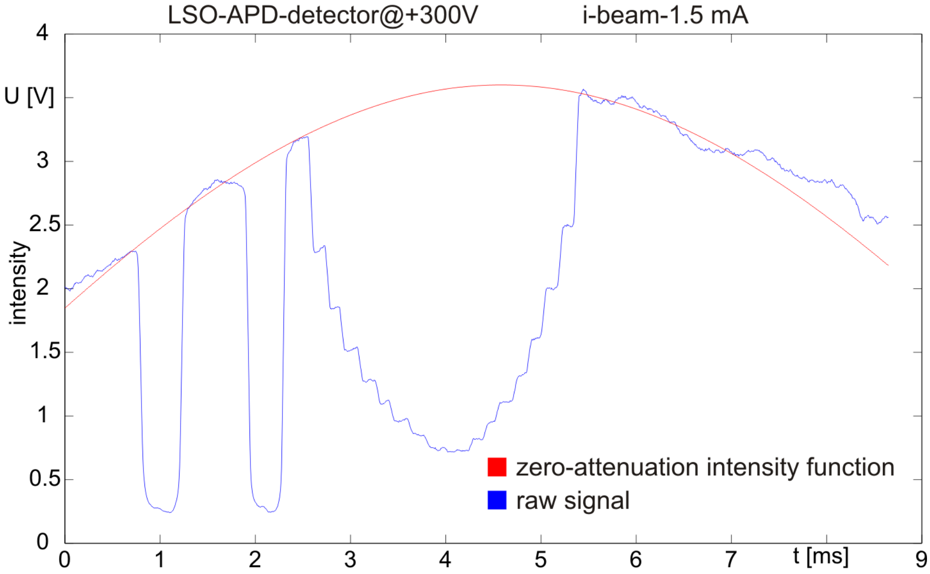

Figure 21: Brass absorber intensity signal with the derived zero-attenuation intensity function.

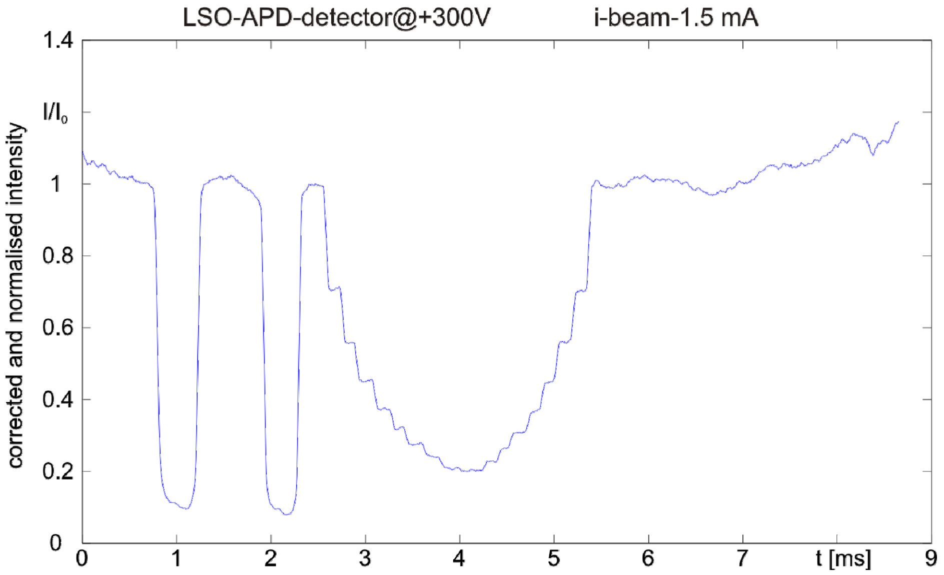

Figure 22: Normalised intensity of brass absorber signal.

From the normalised intensity values the attenuation μx for each of the eight steps of the brass absorber was calculated according to:

$$-\ln I/I_0 = \mu x\,. \qquad (4)$$

The result is presented in Figure 23 where theoretical attenuation curves of brass and aluminium have been added for a better understanding. The data points of μx are of the same order as the calculated attenuation points for brass. However, the characteristic of the measured values follows rather a quadratic behaviour than a strict linear one. Especially for higher values of x (thicker material) there is a visible deviation from the “ideal” curve. This is an effect of beam hardening and scattered radiation. The latter can be explained from Figure 22 where the 30 mm lead absorber should have a normalised intensity of around 0.01 for the given energy spectrum.

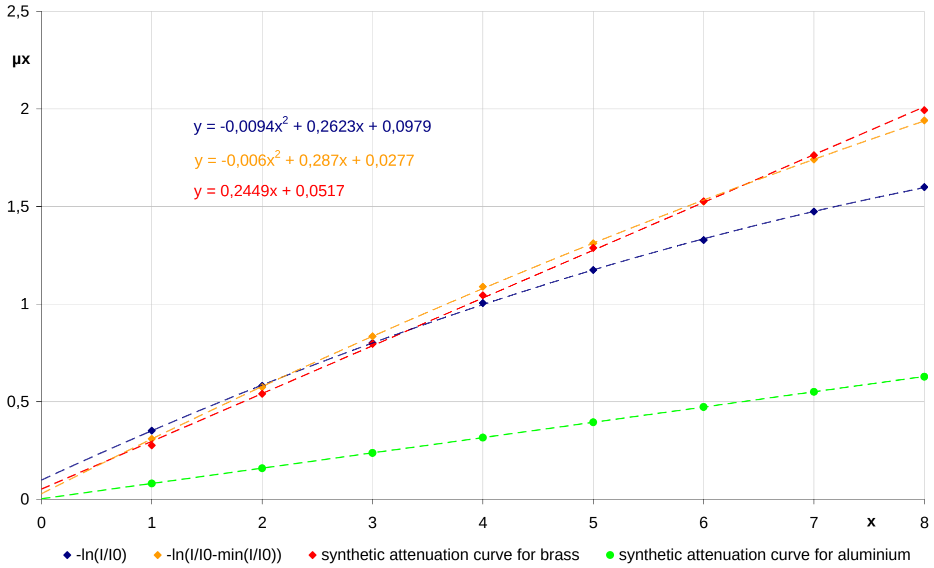

Figure 23: Attenuation chart of the wedge-shaped brass absorber.

To compensate for this scattered radiation an offset was subtracted from the data points (orange data set in the chart). The plotted result is much closer to the synthetic data and the square component of the fitted equation has decreased.

The linearity measurements have shown results within the range of the theoretical values after application of a correction algorithm to the raw data. Discrepancies between the measurements and the synthesised data arise from scattered radiation and beam hardening. The latter effect is gaining more influence with increased material thickness.

For the following tomographic measurements the application of an algorithm to correct the raw data is not applicable due to the amount of data that has to be processed and the experimental setup itself. Consequently distortions due to scattered radiation and beam hardening have to be expected that will affect the contrast of the obtained reconstructed images.

3.5 Tomography of a simple Al-PMMA structure and metal pins

The object of investigation was the PMMA phantom depicted in Figure 24. The outer ring was 6 mm thick aluminium. There were no insets in the PMMA structure. Three small metal pins (∅ 2 mm) were inserted into the phantom to monitor and correct geometrical distortions in the recorded sinogram data. A synthetic sinogram, based on the geometry shown in Figure 24 was generated and compared with the recorded one. The horizontal (temporal) comparison of the two sinograms revealed that the recorded sinogram is distorted horizontally (refer to the aid lines in Figure 25).

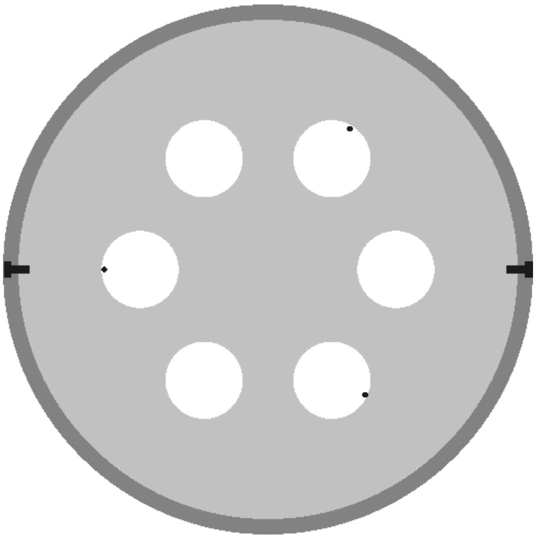

Figure 24: Geometrical model of the reduced Al-PMMA structure.

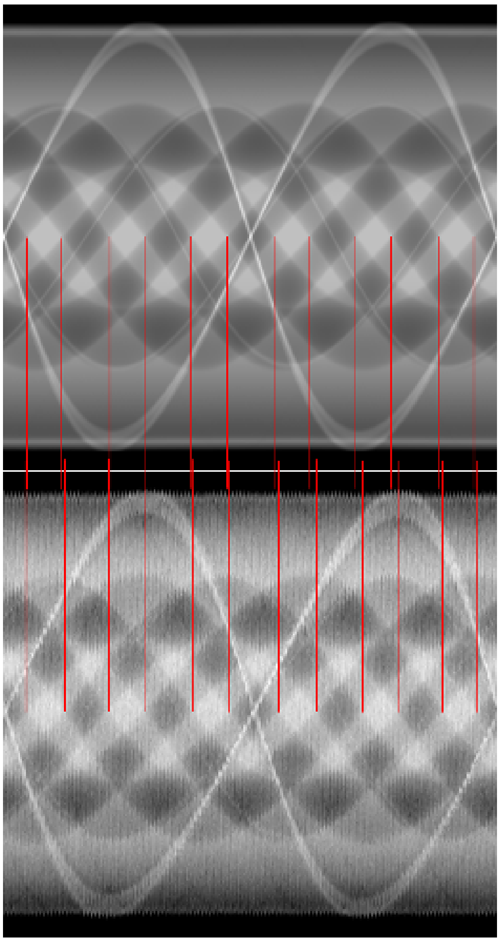

Figure 25: Synthetic (top) and recorded (bottom) sinogram with aid lines.

The source of the horizontal distortion was the inconstant rotation speed of the object that lead to angular oriented image artefacts during image reconstruction. The reconstructed image (Figure 26) has therefore typical displacement artefacts. Moreover there seem to be some radial artefacts as well.

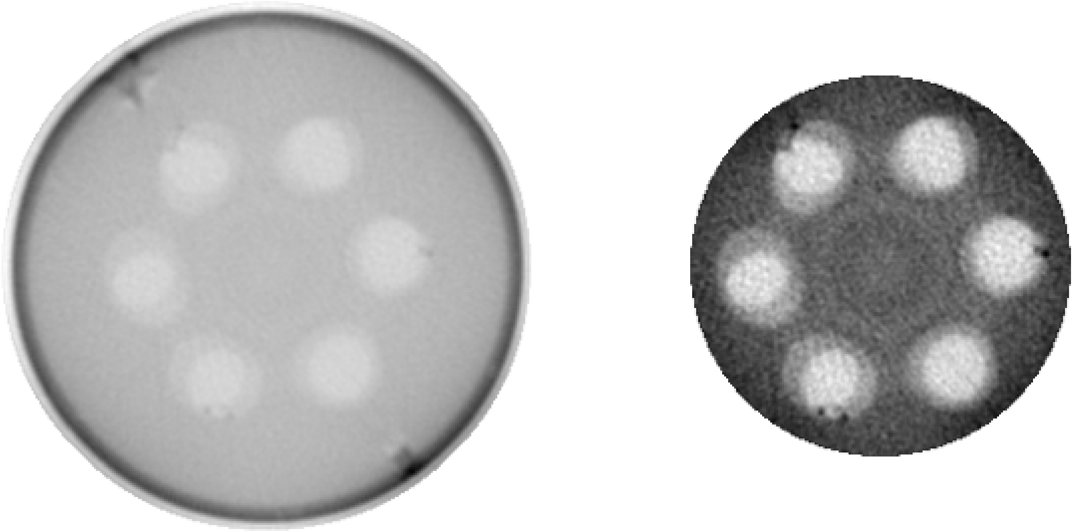

Figure 26: Reconstructed image based on the raw (uncorrected) data.

A shaft encoder attached to the motor provided information about the momentary rotating speed of the object (Figure 27a) during the measurements. Based on the velocity profile given in the picture a corresponding correction function (Figure 27b) was applied to compensate the horizontal distortion of the recorded sinogram. The result of the subsequent reconstruction is depicted in Figure 28.

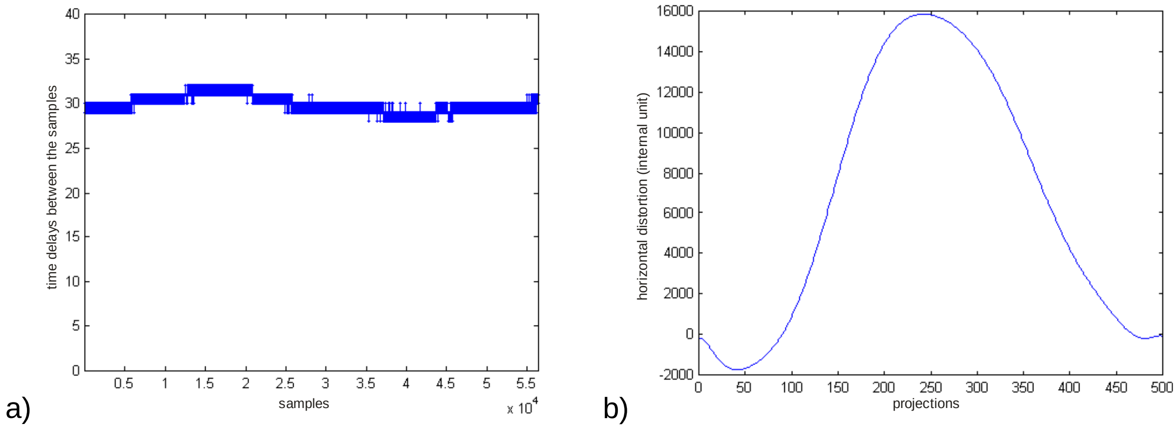

Figure 27: a) Recorded rotating speed of the object and b) derived rotation correction function.

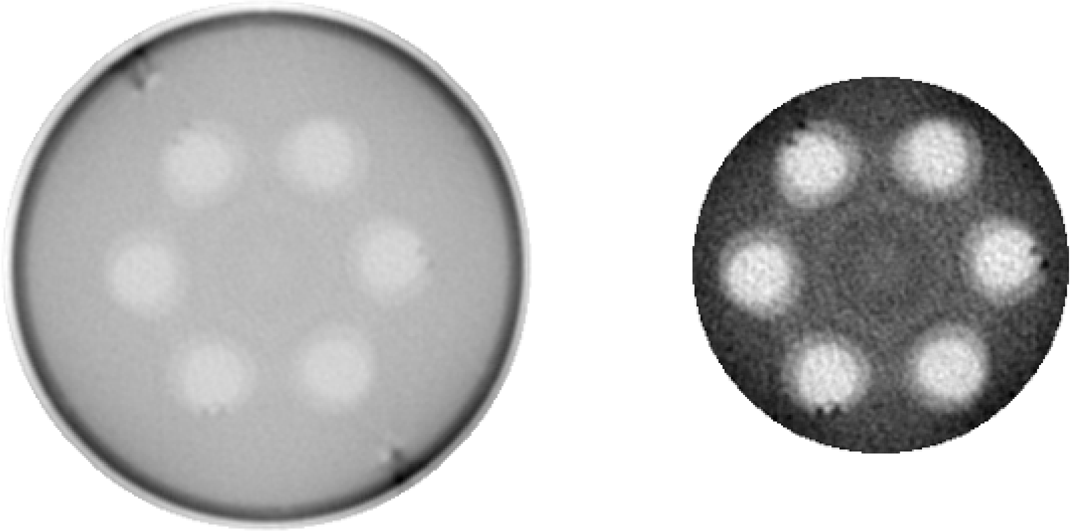

Figure 28: Reconstructed image based on the corrected sinogram.

In comparison to Figure 26 the reconstruction is more symmetric, but the six holes show an unreal diffuse border and the metal pins appear twice. To gain deeper understanding of the problem the synthetic and the recorded sinogram were compared regarding their vertical dimensions (Figure 29).

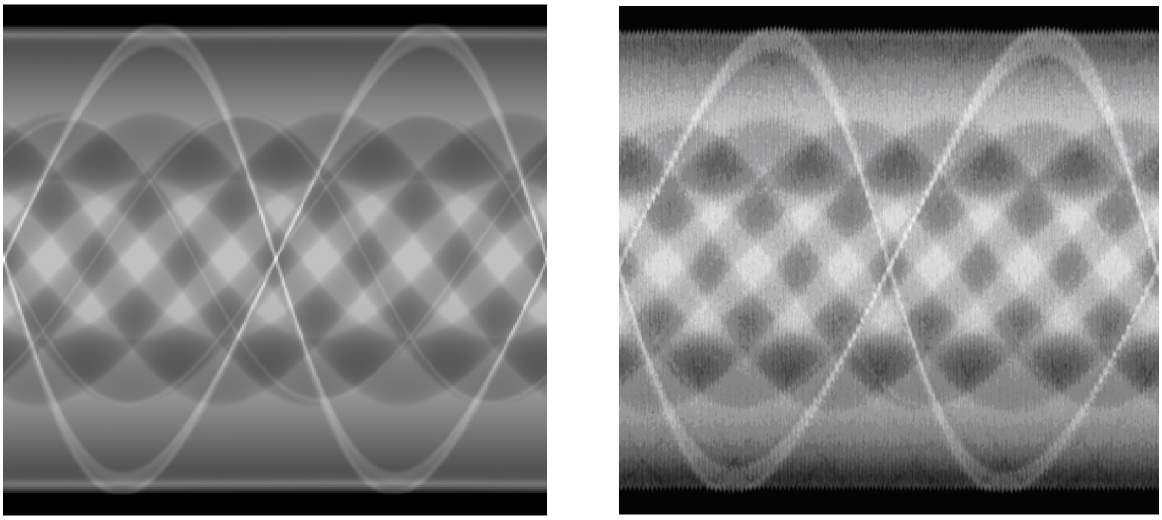

Figure 29: Synthetic (left) and measured (right) sinogram.

The comparison revealed that structures of the objects' periphery were located at the same position whereas inner structures were shifted in the vertical direction.
This could be caused by the following reasons:

- The “detector-centre of rotation” vector was not orthogonal with respect to the target strip during the measurements – an alignment error of about 1° would not cause the observed distortion.
- The target is deformed along the scanning line as depicted in Figure 30
- The beam deflection is not in a steady state.

The area of the target that contributes to possible errors was located between ±150 mm from the target's centre. Within these boundaries the total deformation is about 0.3 mm.

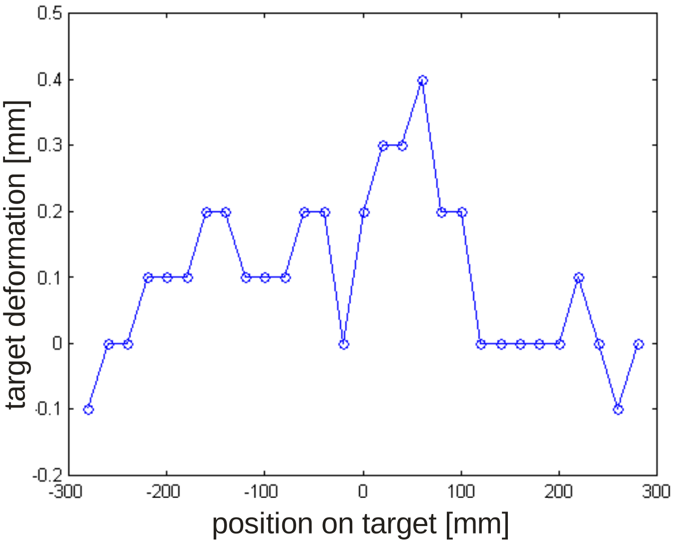

Figure 30: Measured deformation of the target strip that was used for the experiments.

To investigate the influence of an unsteady beam deflection the temporal behaviour of the current which drives the deflection coils was analysed (Figure 31). The current through the coils has a triangular characteristic with small distortions on its shoulders. Subsequent sinograms will be generated only on the basis of the rising part of the signal corresponding to the time-stamps between 2000 and 5000.

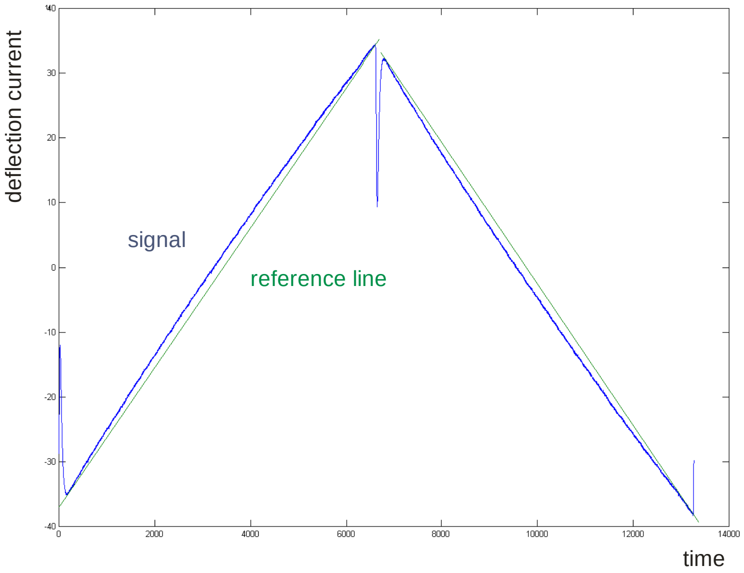

Figure 31: Single period of the deflection current.

To gain a deeper understanding of the temporal beam position a slit mask was placed in front of the target. Without another object in the path of rays a sinogram was obtained as shown in Figure 32.

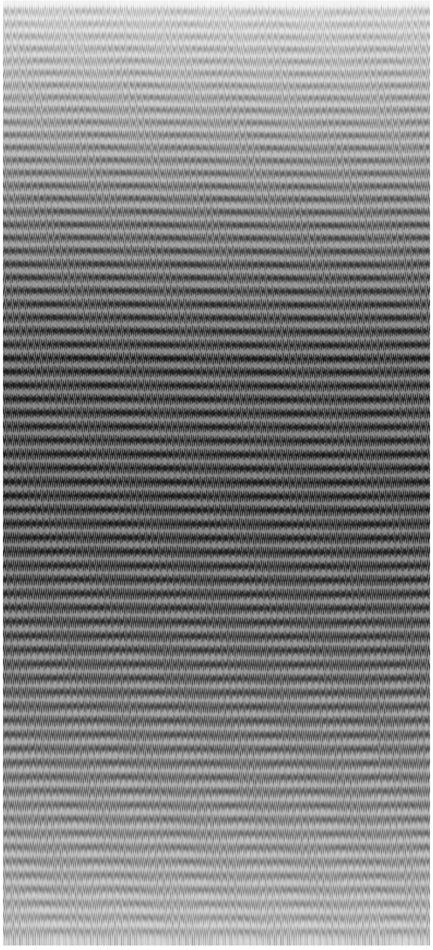

Figure 32: Section of the sinogram – recorded with only a slit mask in the path of rays.

The sinogram reveals that the projections were displaced with respect to each other, and that their widths differed. The origin of those effects was the high voltage source of the electron beam that introduced ripples due to its principle of operation. By knowing the scanner signal it is not possible to gain information about the parasitic frequency and cancel that out since it is not a multiple of the scanning frequency. Under the given conditions it would be necessary to analyse every single projection and consequently it would be necessary to constantly use the slit mask. This, however, would introduce artefacts during the tomographic reconstruction.

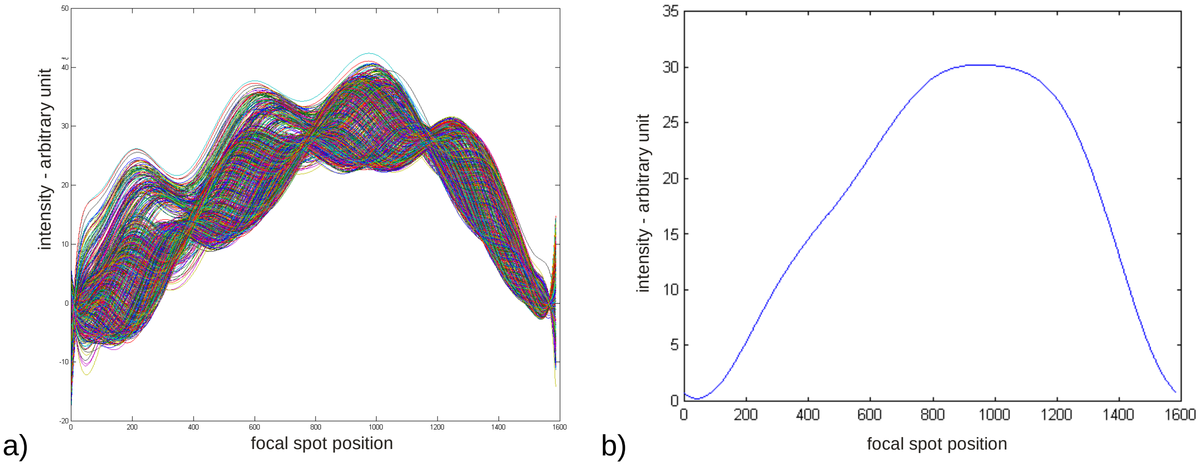

Figure 33: a) Analysis of a complete sinogram obtained from the slit mask records and b) filtered and averaged signal over all projections.

The analysis of the measurements containing the slit mask (Figure 33) are still of interest since they allow to gain a filtered and averaged signal over all projections. In order to reduce vertical deformations of the recorded sinogram the information from Figure 30 and Figure 33b were processed and the correction function depicted in Figure 34 was obtained.

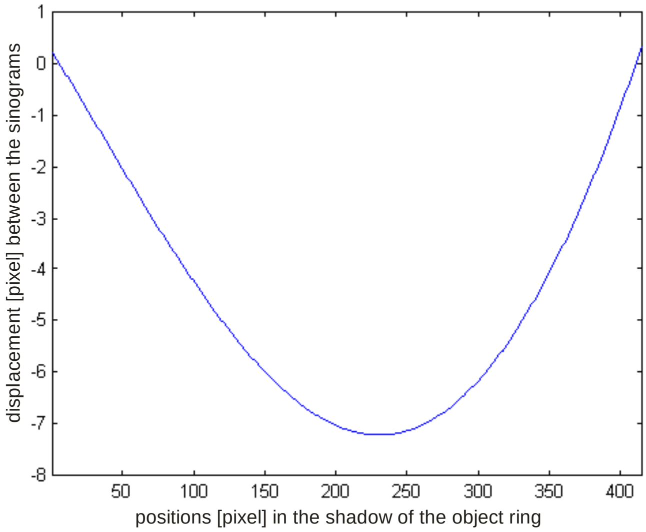

Figure 34: Waveform to correct vertical disdistortions within the sinogram.

The two-dimensional correction of the sinogram (horizontal and vertical) is the basis for the reconstructed image shown in Figure 35.

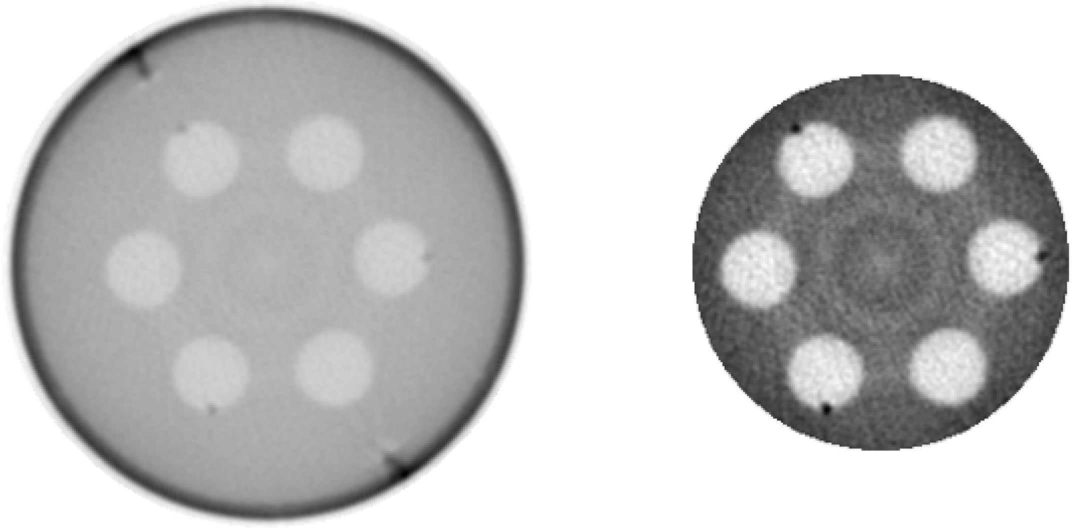

Figure 35: Reconstructed image after application of the correction functions.

3.6 Tomography of a simple Al-PMMA structure and metal insets

The object of investigation is the PMMA phantom with a 6 mm thick aluminium ring and four metal insets placed inside the holes of the PMMA: copper, brass, steel and aluminium. The holes on the left and right side are empty. The slit mask was used during that experiment. This caused concentric rings in the reconstructed images and reduced the image quality. Therefore the slit mask was not used during the following measurements.

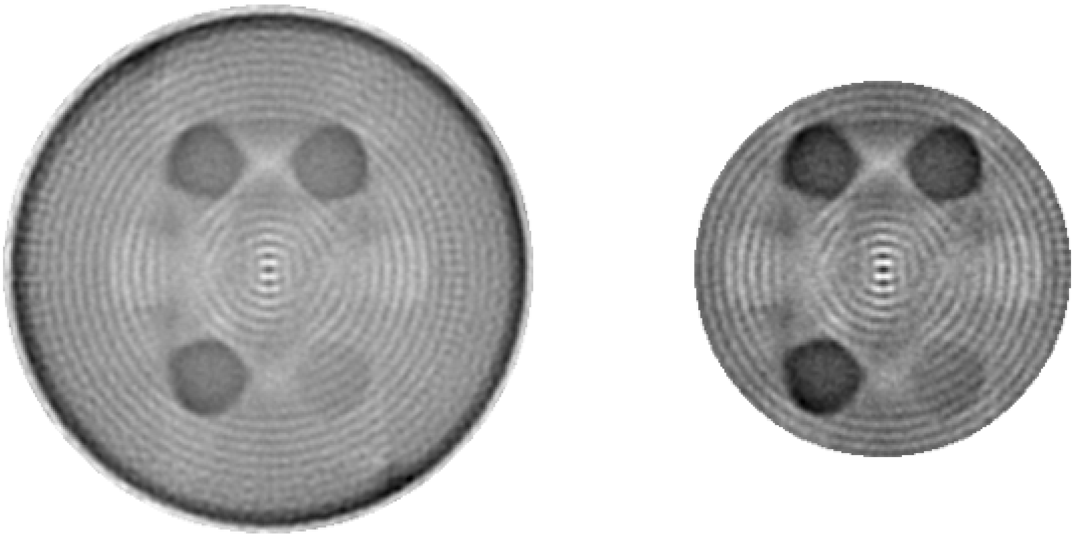

Figure 36: Reconstructed image of the Al-PMMA structure with metal insets and the slit mask, recorded at 0.6 mA beam current.

The reconstructed images without the slit mask are depicted in Figure 37. The artefacts at the boundaries of the metal insets (bright and dark “flags” as well as the non-circular appearance of the insets) are caused by beam hardening and scattered radiation.

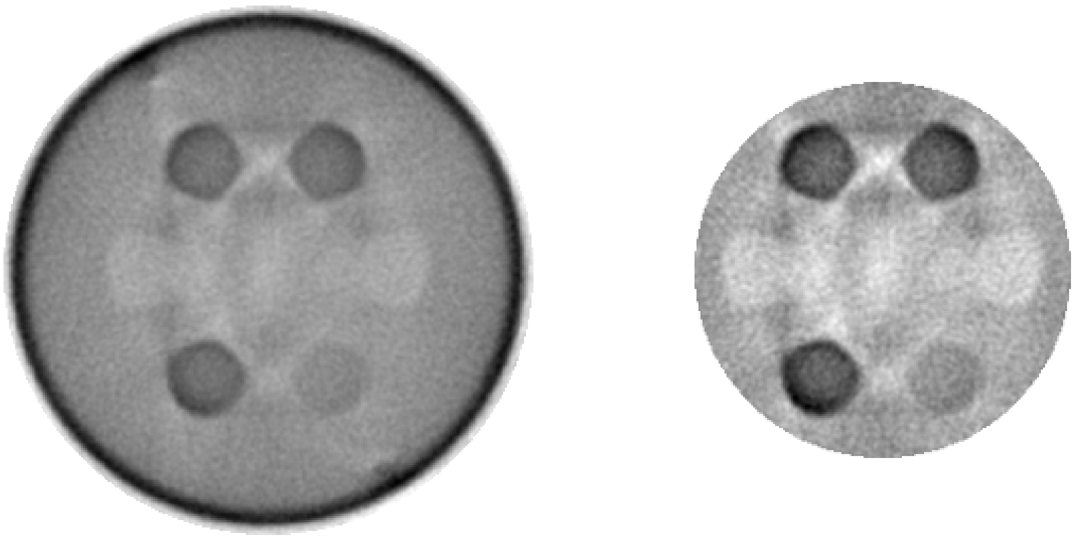

Figure 37: Reconstructed image of the Al-PMMA structure with metal insets, inset, recorded at 0.6 mA beam current.

It seems that the attenuation within the aluminium is only fractionally larger than in the surrounding PMMA. In contrast the attenuation in the other metal insets is much higher. The beam current was set to 0.6 mA. The consequence is the stronger appearance of noise within the images in comparison to the following images that were recorded at higher beam currents. Furthermore problems related to non-linear attenuation of the X-rays could be emphasised due to a low incident intensity (refer to chapter 3.4).

3.7 Tomography of a simple Al-PMMA structure and drilled Al-inset

The object of investigation is the same as above but with an additional drilled aluminium inset. The holes have a diameter of 3 mm. The drill pattern is shown in Figure 38 a). The minimum wall thickness due to the holes is 0.9 mm. The first two drillings from the left are just distinguishable whereas the next drilling can be easily distinguished.
The following measurement was performed at a beam current of 2 mA (Figure 40). Hence the noise level decreased significantly in comparison to the first measurement at a beam current of 1 mA (Figure 39).

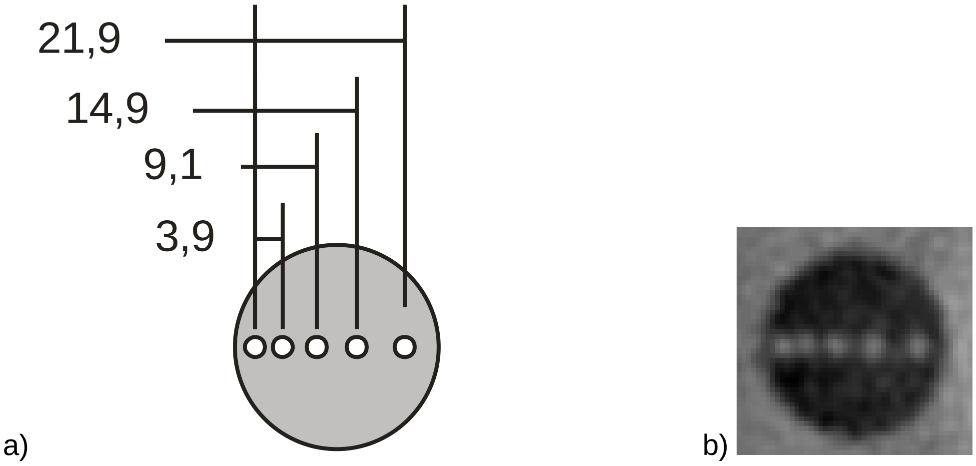

Figure 38: Drilled aluminium inset (drill hole diameter of 3 mm), a) schematic and b) reconstructed image.

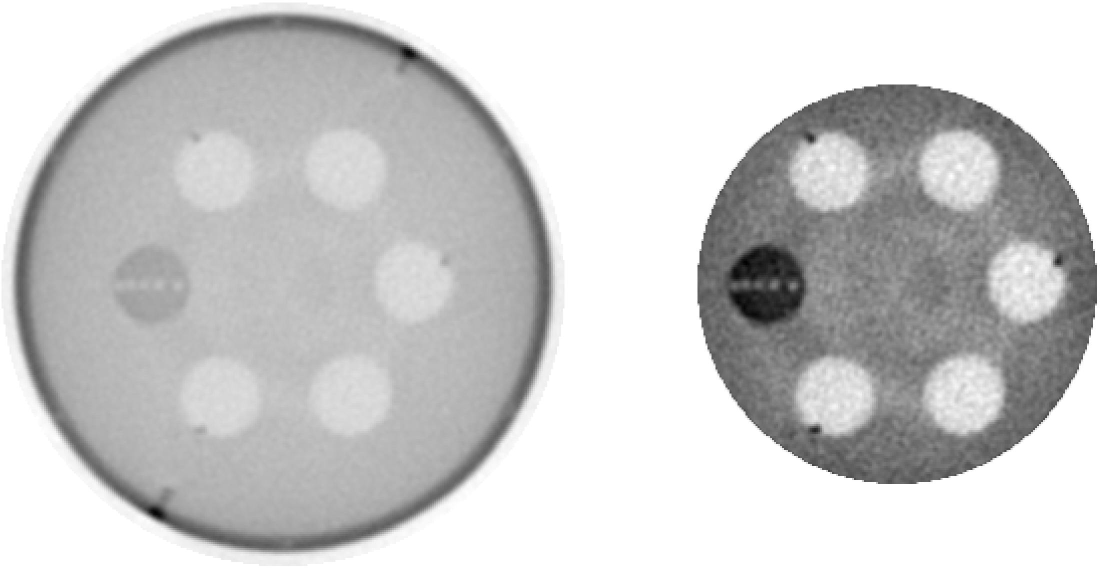

Figure 39: Reconstructed image of Al-PMMA structure with drilled Al-inset recorded at 1 mA beam current.

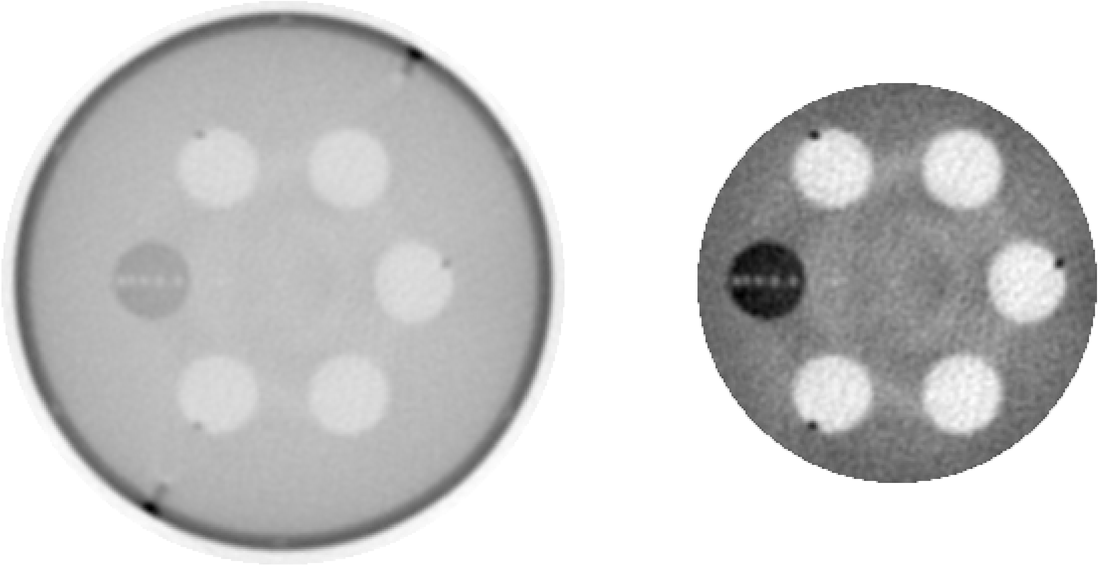

Figure 40: Reconstructed image of Al-PMMA structure with drilled Al-inset recorded at 2 mA beam current.

3.8 Tomography of a fuel element phantom

The object of investigation is the fuel element phantom depicted in Figure 8 with a 6 mm thick aluminium ring. The result of the reconstruction is presented in Figure 41. In order to obtain a more detailed view of the phantom the beam current was increased to 5 mA and the result is shown in Figure 42.

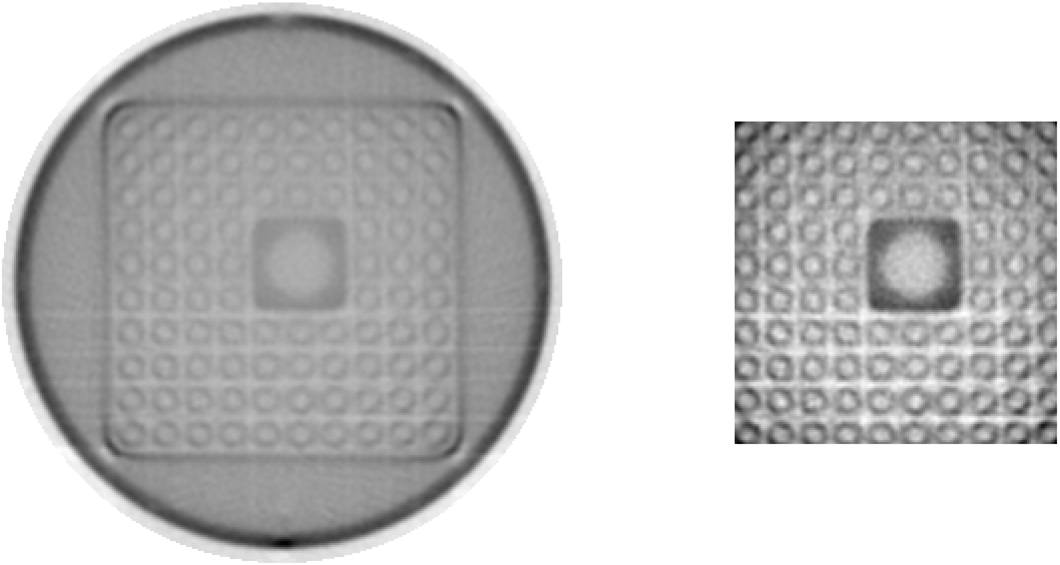

Figure 41: Reconstructed image of a fuel element phantom, recorded at 2 mA beam current.

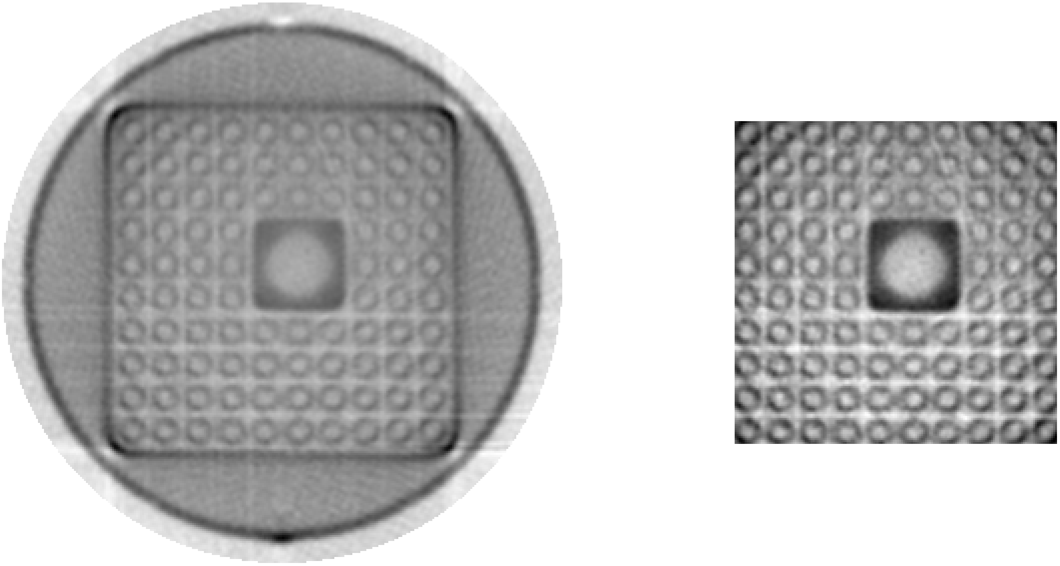

Figure 42: Reconstructed image of a fuel element phantom, recorded at 5 mA beam current.

The increase of the beam current did cancel out some noise but it could not reveal the structures within the PMMA. Only the difference between the upper and lower half of the fuel element (PMMA and air) are distinguishable now, as can be seen in an illustration with extended grey values (Figure 43).

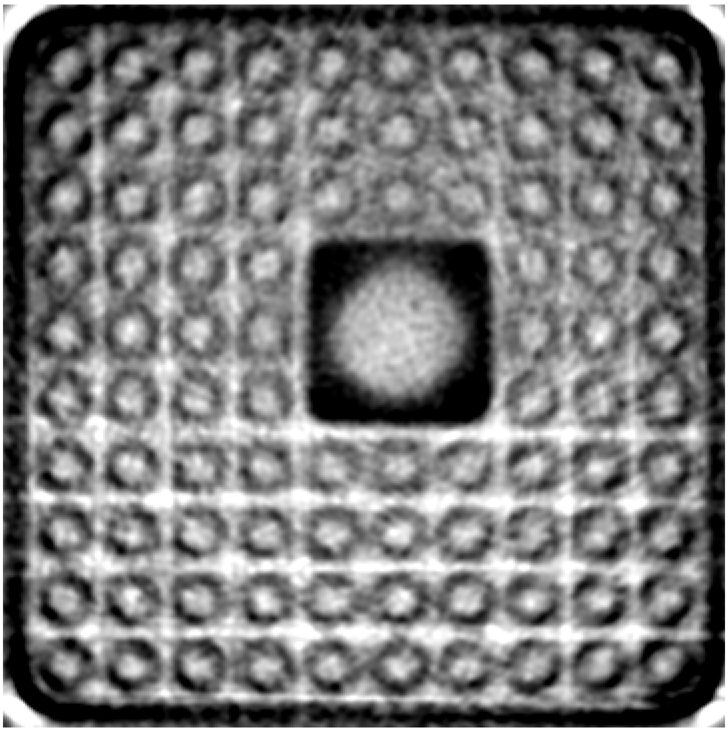

Figure 43: Section of reconstructed fuel element with extended grey values.

The reason for missing details within the PMMA structure might be:

- Insufficient correction of the sinogram
- Low photon flux at the detector due to high absorption
- “Radiation specific” artefacts, such as beam hardening and scattered radiation.

4 Summary

The project has proven the principle feasibility of a high energy X-ray tomography setup based on a 1 MeV ELV-6 (BINP) electron accelerator and a single detector. The experimental setup was kept as simple as possible but still allowed for tomographic measurements.

The electron beam focal spot size was found to be 0.7 mm ±0.1mm FWHM. Repeat accuracy was analysed and a maximum dislocation of the beam of 6 mm was detected.

The issue of the detector's SNR could only be addressed partially since the measured noise level is a combination of noise coming from the detector and noise originating in the accelerator. The maximum SNR, combining both – noise from the detector and accelerator, was 40.5 dB.

Tomographic measurements have been carried out successfully with different beam configurations and phantoms. Geometrical details down to 2 mm in size (metal pins) were clearly distinguishable.

A major problem is still the unwanted beam position fluctuation due to uncompensated high-voltage ripple. This effect reduces spatial resolution and contrast considerably, making it partly impossible to discriminate small low-contrast inclusions, such as plastic pins and holes in plastics. Furthermore future work should encompass reduction of beam hardening and scattered radiation effects.

List of abbreviations

Abbreviation	**Meaning**
APD	avalanche photo diode
BINP	Budker Insitute of Nuclear Physics
CdTe	cadmium telluride
CT	computed tomography
FWHM	full width at half maximum
FZD	Forschungszentrum Dresden Rossendorf
kS/s	kilosamples per second
LSO	lutetium oxyorthosilicate
PMMA	polymethyl methacrylate
rpm	revolutions per minute
SNR	signal-to-noise ratio
USB	universal serial bus

References

[1] U. Hampel et al., “Experimental ultra fast X-ray computed tomography with a linearly scanned electron beam source,” *Flow Measurement and Instrumentation*, vol. 16, no. 2, pp. 65-72, 2005.

[2] F. Fischer et al., “An ultra fast electron beam x-ray tomography scanner,” *Measurement Science and Technology*, vol. 19, no. 9, p. 094002, 2008.

[3] V.G. Cherepkov et al., “Accelerators of the ELV-type and their use in radiation-technological processes”, *Science for Manufacture*, special issue, p.5-10, 2004.

Index of figures and tables